Food &
Function

PAPER

View Article Online
View Journal | View Issue

Cite this: *Food Funct.*, 2022, **13**, 11770

Astaxanthin attenuates irradiation-induced osteoporosis in mice by inhibiting oxidative stress, osteocyte senescence, and SASP

Qinghe Geng, *[a,b,c] Shen Wang,[d] Ke Heng,[e] Juan Zhai,[c] Xingchen Song,[c] Lei Xia,[f] Lulu Wang,[f] Qiang Lin,[g] Hongwei Li[g] and Yilong Guo*[c]

Received 25th June 2022,
Accepted 26th September 2022

DOI: 10.1039/d2fo01673g

rsc.li/food-function

Radiation therapy (RT) is a crucial part of many treatment plans for cancer patients. However, major undesired side effects are associated with this treatment, including impaired bone remodeling and bone loss. Irradiation induces bone loss due to promoted osteoclastic bone resorption and reduced osteoblastic bone formation. Astaxanthin (AST) is a natural antioxidant with anti-oxidative and anti-aging properties. However, it is unclear whether AST is also protective against osteoporosis induced by ionizing radiation (IR). Here, we evaluate the efficacy of AST in mitigating IR-induced bone loss in a mouse model where both hindlimbs received radiation. Reduced BMD, bone biomechanical strength, bone formation, elevated oxidative stress, and osteoclast activity with microarchitectural deterioration of trabecular and cortical bones were observed in IR mice. Supplementation with AST corrected these osteoporotic phenotypes, caused by IR, by inhibiting oxidative stress, DNA damage, osteocyte senescence, and senescence-associated secretory phenotype (SASP), subsequently promoting osteoblastic bone formation and inhibiting osteoclastic bone resorption. The results from our study provide experimental evidence for the clinical use of AST to prevent IR-induced osteoporosis in cancer patients.

Introduction

Radiation therapy (RT), using ionizing radiation (IR), has been demonstrated to be effective in killing cancer cells and reducing tumor size and is one of the most common treatment modalities for cancer patients. However, the use of RT is commonly associated with normal adjacent tissue injury.[1] IR reduces the survival of bone marrow stromal cells,[2] decreases blood supply, and induces partial oxygen pressure in surrounding tissues, leading to a substantial reduction in bone quantity and quality.[3,4] Animal studies have also demonstrated that RT increases the number of osteoclasts and elevates the circulating markers of bone resorption (TRAP5b) in mice,[3,5–7] leading to significant trabecular bone loss.[8] In addition, IR also reduces serum bone formation markers (osteocalcin), bone mineral density (BMD), and *ex vivo* osteoblast differentiation in mice.[9] Therapeutic doses of IR have been found to have severe adverse side effects in terms of bone health in patients.[10] Accumulating clinical studies have confirmed that RT leads to lower BMD, enhanced fragility, and increased fracture risk in cancer survivors. After RT, rib fracture rates increase 10-fold in breast cancer patients.[11–15] Therefore, there is an urgent need to explore the molecular mechanisms driving this and to identify medical interventions capable of attenuating or preventing IR-related bone loss.

Thanks to extensive studies in animals, we have a deeper understanding of the changes that occur inside the bone microenvironment upon exposure to IR, many of which are similar to age-related osteoporosis.[16] Growing evidence suggests that cellular senescence is a strong contributor to the development of age-related diseases, including osteoporosis.[17] A hallmark of age- and IR-related bone loss appears to be the chronic accumulation of senescent cells.[16–18] Senescence is a stress response that suppresses the proliferation of damaged cells, causing them to enter a state of irreversible growth arrest even in the presence of growth stimuli and oncogenic insults.[19–22] Despite being in a dysfunctional internal environ-

---

[a] *Cancer Institute, Xuzhou Medical University, Xuzhou, China. E-mail: Qinghe Geng@xzhmu.edu.cn*
[b] *Center of Clinical Oncology, Affiliated Hospital of Xuzhou Medical University, Xuzhou, China*
[c] *Central Lab, Pizhou Hospital, Xuzhou Medical University, Xuzhou, China. E-mail: Guoyilong888@163.com*
[d] *Peking University People's Hospital, Beijing, China*
[e] *Department of Orthopedics, Changzhou Second Hospital, Nanjing Medical University, Changzhou, China*
[f] *Department of Pathology, Affiliated Hospital of Xuzhou Medical University, Xuzhou, China*
[g] *Department of Orthopedics, Affiliated Hospital of Xuzhou Medical University, Xuzhou, China*

ment, senescent cells remain metabolically active and have heightened survival capabilities, making them highly viable and resistant to apoptosis.[23] Senescent cells can secrete proinflammatory cytokines, extracellular matrix proteins, and chemokines, which together produce a toxic microenvironment termed the senescence-associated secretory phenotype (SASP).[24–26] By spreading toxic factors to neighboring bystander cells, SASP likely contributes to additional senescent cell accumulation and further tissue dysfunction.[27] SASP also results in harmful paracrine effects as well as systemic effects.[25–27] Cellular senescence has been suggested to be an important contributor to the development of age-related diseases *via* its growth arrest phenotype in addition to SASP. Senescent cells produce a pro-inflammatory secretome that results in decreased bone formation and increased bone resorption, and therapies that either clear senescent cells or suppress the production of SASP have been shown to attenuate or prevent bone loss in mice.[28,29]

Astaxanthin (AST) is a red carotenoid pigment that is found in some seafoods, such as trout, salmon, crab, shrimp, and other aquatic animals.[30] Astaxanthin has unique chemical properties due to its molecular structure. The presence of hydroxyl and keto moieties on each ionone ring has been postulated to result in its high antioxidant activity.[31] As a potent antioxidant, AST exhibits a variety of biological activities, such as preventing ischemia-reperfusion injury,[32] asthma,[33] liver damage,[34] and neuroinflammation.[35] In AST-treated mice, the expression of many genes related to oxidative stress was shown to be inhibited.[36] AST treatment was also shown to significantly attenuate alveolar bone loss by increasing osteoblastic bone formation and reducing osteoclastic bone resorption in an experimental periodontitis model.[37] AST also reduced osteoclastic bone resorption and bone loss in OVX model mice.[38] However, the protective effect of AST against IR-induced osteoporosis has not been studied yet.

The radiation-exposure mouse model is a mature and widely used animal model in the study of irradiation-induced osteoporosis.[16,39] Thus, we investigated the role and potential mechanisms of AST in irradiation-induced osteoporosis using this radiation-exposure mouse model. We examined alterations in bone tissue changes by measuring bone microarchitecture, bone dynamics, bone mass, bone turnover, and bone biomechanical strength parameters. Moreover, we analyzed tissue-level changes in osteoblast and osteoclast activity, oxidative stress, DNA damage, osteocyte senescence and SASP.

Materials and methods

Experimental design

All animal procedures were performed in accordance with the guidelines set out by the Chinese Ministry of Science and Technology Guide for the Care and Use of Laboratory Animals. All procedures in this study were approved by the Institutional Animal Care and Use Committee of Pizhou Hospital (Pizhou, China). Thirty 12-week-old male C57BL/6J mice were purchased from Jackson Laboratory (Beijing, China). Ten mice were used as a blank control (Con) group and 20 mice were randomly divided and assigned to IR exposure (IR) and IR exposure with AST supplementation (IR + AST) groups ($n = 10$). Three mice were housed in each cage and allowed free access to tap water and chow. Animals were housed under controlled temperature (23 ± 1 °C) and relative humidity (50%–60%) conditions. The Con and IR group mice were fed a standard AIN-93G Diet (17.2% kcal from fat, 18.8% kcal from protein, and 63.9% kcal from carbohydrate). The diet for IR + AST mice contained 0.1% AST (Sigma-Aldrich Co., USA) mixed in the standard mouse chow.[40]

Double labeling of bone with calcein (8 mg kg^{-1}, Sigma-Aldrich, USA) was performed on days 2 and 12 before sacrifice. The animals were euthanatized with an overdose of anesthetic chloral hydrate (2 mL per 100 g of body weight) at the end of the 12-week experiment. Serum samples were obtained *via* abdominal aorta puncture and were then centrifuged for 10 min at 4000*g* and stored at −80 °C for biochemical analysis. The bilateral hindlimbs were harvested and then immediately wrapped in saline-soaked gauze and stored at −80 °C. The right femurs were subjected to DXA, μCT scanning and dynamic bone histomorphometry. The right tibias were fixed in 4% neutral-buffered formalin for static bone histomorphometry. The left femurs were used for three-point bending and nanoindentation tests, while the left tibias were stored in liquid nitrogen for western blot and qRT-PCR analyses.

Radiation exposure

Mice were anesthetized using isoflurane (induction 3%, maintenance 1.5%, and oxygen flow 3 L min^{-1}) and secured on a platform for irradiation exposure. Briefly, both hindlimbs from each mouse were irradiated (20 Gy, single dose, anterior) with 300 kVp X-rays at a rate of 2.4 Gy min^{-1} using a linear accelerator at Pizhou Hospital (Pizhou, China).[41]

Serum biochemical analysis

The serum bone formation marker alkaline phosphatase (ALP, U L^{-1}) and procollagen type 1 intact N-terminal propeptide (P1NP, U L^{-1}), and bone resorption markers, such as C-terminal cross-linked telopeptides of type 1 collagen (CTX-1, ng mL^{-1}) and tartrate-resistant acid phosphatase 5b (TRACP5b, U L^{-1}), were detected using commercial enzyme-linked immunosorbent assay (ELISA) kits (Jiancheng Biotech Co., Nanjing, China) in the mice from different groups ($n = 10$ for each group). These analyses were performed according to the protocols provided by the supplier.

DXA analysis

At the end of treatment, the mice were sacrificed and their left femurs were dissected free of tissue and fixed in 4% neutral-buffered formalin. The BMD and BMC of the tibia, femur, spine, and total body *in vivo* were analyzed by dual-energy X-ray absorptiometry (DXA, Lunar Corp., Madison, USA) as previously reported.[39,42,43]

Three-point bending test

A commercial mechanical testing device (Bose ElectroForce 3220; Bose Corp., USA) was used to analyze the whole-bone structural properties of the left femurs of mice ($n = 10$ from each group) as previously reported.[39,42,43] Load–displacement curves were simultaneously plotted and the data were automatically acquired. The parameters, including maximum load (N), yield load (N), ultimate displacement (μm), yield displacement (μm), stiffness (N/mm), and energy absorption (N× mm), were acquired from these load–displacement curves.

Nanoindentation

After the cleaning process, the femurs were mounted on a nanoindentation system (Agilent G200, Agilent Technologies Inc., USA). A force–displacement curve was automatically recorded and the trabecular bone elastic modulus (GPa) and contact hardness (GPa) were calculated according to previously described methods.[39,42,43]

Micro-computed tomography analysis

Right femurs ($n = 10$ for each group) were scanned with a high-resolution μCT (Skyscan1172, Belgium). After scanning, the 2D image sequences were automatically reconstructed into 3D volumes with a 7 μm isotropic voxel size (55 kVp, 145 μA). All 3D manipulations and analyses were performed using the NRecon software (Skyscan, Belgium). The trabecular bone parameters, including trabecular bone volume/total volume (BV/TV, %), trabecular number (Tb.N, 1/mm), trabecular thickness (Tb.Th, μm), trabecular bone surface/bone volume (BS/BV, 1/mm), and trabecular spacing (Tb.Sp, μm), were determined. The cortical thickness (Ct.Th, μm), cortical volume (Ct.V, mm^3), and cortical area (Ct.Ar, mm^2), which are three major cortical bone parameters, were also analyzed.[39,42,43]

Histology and histomorphometry

After μCT scanning, the femoral samples were fixed in 80% ethanol for 24 h and then embedded in methylmethacrylate. The unstained femoral samples were then imaged using fluorescence microscopy (Leica SP5, Germany) to observe and quantify the dynamic trabecular bone histomorphometric parameters ($n = 10$ for each group), including mineral apposition rate (MAR, μm day^{-1}), mineralizing surface/bone surface (MS/BS, %), and bone formation rate/bone surface (BFR/BS, $\mu m^3\ \mu m^{-2}\ day^{-1}$).

The right tibial samples after dissection were fixed in 4% PFA, decalcified in 10% ethylenediamine tetraacetic acid (EDTA), and then embedded in paraffin. Five-μm-thick sections were stained with HE, Von Kossa, ALP, and toluidine blue to assess osteogenesis and then stained with TRAP to detect osteoclastogenesis. Static trabecular bone histomorphometric parameters, including trabecular bone volume/total volume (BV/TV, %), osteoblast number/millimeter of trabecular bone surface (N.Ob/BS, 1/mm), and osteoclast number/millimeter of trabecular bone surface (N.Oc/BS, 1/mm), were quantified for each sample ($n = 10$ for each group).

RNA isolation and quantitative real-time RT-PCR

After animal sacrifice, the soft tissues and muscles from the left tibias ($n = 10$ for each group) were carefully removed. Total RNA was isolated using the TRIzol reagent (Invitrogen, Carlsbad, USA). After denaturation of total RNA at 70 °C for 5 min, cDNAs were synthesized from total RNA using an oligo dT primer by reverse transcription (Promega, USA). Quantitative real-time PCR was performed using SYBR Green PCR Master Mix (Qiagen, USA) with an ABI PRISM 7900 sequence detector (Applied Biosystems, USA) according to the manufacturer's instructions. Samples were plotted relative to a standard curve generated by amplifying serially diluted products using the same PCR reactions. The housekeeping gene glyceraldehyde-3-phosphate dehydrogenase (GAPDH) served as an internal control. Primers were synthesized by Nanjing Genscript Biological Engineering Technology & Service Co., Ltd (Nanjing, China). The primers used in this study are shown in Table 1.

Immunohistochemistry

Immunohistochemical staining was carried out as described previously[42] for P16INK4a, P21, P53, and senescence-associated β-galactosidase (SA-β-gal), using the avidin–biotin-peroxidase complex technique with affinity-purified rabbit anti-mouse P16INK4a (ab108349), SA-β-gal (ab130804), P21 (ab188224), and P53 (ab227655).

Western blot analysis

For the examination of protein expression levels, proteins were extracted from bone tissue and then quantitated with a protein assay kit (Bio-Rad, Mississauga, Ontario, Canada). The protein samples (15 μg) were then fractionated by SDS-PAGE and transferred to nitrocellulose membranes. The membranes were blotted with primary antibodies against p16 (ab16123), p21 (ab86696), p53 (ab26), SA-β-gal (ab136716), Sirt1 (ab110304), Prdx1 (ab109498), SOD1 (ab51254), or γH2AX (ab81299). β-Actin (ab6276) was used as a loading control. Immunoblotting was carried out as described previously.[42]

Statistical analyses

All data are provided as the mean ± standard deviation (SD). Statistical analyses were performed using GraphPad Prism 8.0 software (GraphPad Software, CA, USA). Comparisons between experimental groups were made using the one-way ANOVA test. A level of $P < 0.05$ was considered significant and reported in each graph.

Results

AST attenuates BMD and BMC reduction in IR mice

To assess the effects of AST on bone mass in IR mice, the bone mineral density (BMD) and bone mineral content (BMC) in these mice were measured by DXA. The BMD and BMC values of the tibia, femur, spine, and total body decreased significantly after IR (Fig. 1A). As expected, AST treatment nearly

Table 1 Sequences of primers employed for RT-PCR

Name	Forward	Reverse
ALP	CCTAGACACAAGCACTAACACTA	GTCAGTCAGGTTGTTCCGATTC
BMP2	GAATGACTGGATCGTGGCACCTC	GGCATGGTTAGTGGAGTTCAGGTG
COL-1	CCCTACTCAGCCGTCTGTGC	GGGTTCGGGCTGATGTACC
OCN	GCCTTCATGTCCAAGCAGGA	GCGCCGGAGTCTGTTCACTA
OSX	CATCTAACAGGAGGATTTTGGTTTG	AAGCCTTTGCCCACCTACTTTT
RUNX2	CTGTGGTTACCGTCATGGCC	GGAGCTCGGCGGAGTAGTTC
CTSK	CTTCCAATACGTGCAGCAGA	TCTTCAGGGCTTTCTCGTTC
TRAP	CACTCCCACCCTGAGATTTGT	CCCCAGAGACATGATGAAGTCA
RANKL	CAGCATCGCTCTGTTCCTGTA	CTGCGTTTTCATGGAGTCTCA
OPG	ACCCAGAAACTGGTCATCAGC	CTGCAATACACACACTCATCACT
SOD1	CGTCATTCACTTCGAGCAGAAGG	GTCTGAGACTCAGACCACATA
SOD2	GGCCAAGGGAGATGTTACAA	GCTTGATAGCCTCCAGCAAC
GPX1	GGGACCTCGTGGACTGGTGGTGCT	CCCGCCACCAGGTCGGACGTACT
GPX2	CGCCTGGTAGTTCTCGGCTTCCCTT	GGGCTGGTACCCACCCCCAGGT
Txnrd1	CAGCGAGGAGACCATAGAGG	GCACATTGGTCTGCTCTTCA
Prx2	ACGAGCATGGGGAAGTTTGT	GCCTTTCCTGGGTCAGCATA
Prx4	GTTACCAACGAAACCGGCG	CCCAATCCTCCTGCTTTACGA
HO1	GAGGCTAAGACCGCCTTCCT	TTGTGTTCCTCTGTCAGCATCAC
Catalase	GTGCCCCCAACTATTACCCC	GAATGTCCGCACCTGAGTGA
NQO1	GAAGACATCATTAAACTACGCC	GAGATGACTCGGAAGGATACTG
NRF2	GCCTTGTACTTTGAAGACTGTATGCA	AAGCGACTCATGGTCATCTACAAAT
Klotho	TGTGAATGAGGCTCTGAAAGC	GAGCGATCACTAAGTGAATACG
IL-1a	CGAAGACTACAGTTCTGCCATT	GACGTTTCAGAGGTTCTCAGAG
IL-1b	CTGGTACATCAGCACCTCAC	AGAAACAGTCCAGCCCATAC
IL-6	TGTATGAACAACGATGATGCACTT	ACTCTGGCTTTGTCTTTCTTGTTATCT
IL-8	AACTTCTCCACAACCCTCTG	TTGGCAGCCTTCCTGATTTC
HGF-1	GGGGACGATACTGTCCTGAA	GTCCCTCAGTGCACATCTCA
MMP3	CAAAACATATTTCTTTGTAGAGGACAA	TTCAGCTATTTGCTTGGGAAA
MMP13	ACTTTGTTGCCAATTCCAGG	TTTGAGAACACGGGGAAGAC
TNF-a	AGTGACAAGCCTGTAGCCC	GAGGTTGACTTTCTCCTGGTAT
P16	CCCGATTCAGGTGATGATGAT	GCGGGAGAAGGTAGTGG
MCP-1	TCACCTGCTGCTACTCATTC	AGTGGATGCATTAGCTTCAG
GAPDH	TGGATTTGGACGCATTGGTC	TTTGCACTGGTACGTGTTGAT

completely abrogated the negative effects of IR on BMD and BMC (Fig. 1A). These results suggested that AST worked effectively to counteract osteoporosis caused by IR.

AST attenuates microarchitecture deterioration in IR mice

Representative μCT images of the left femur from the three groups are shown in Fig. 1B. The IR group mice show a significant alternation of both the cortical and trabecular microarchitecture. IR reduced most bone parameters tested, including BV/TV, Tb.N, Tb.Th, Conn.D, Ct.Th, Ct.V, and Ct.Ar, while increasing Tb.Sp and SMI. However, these parameters were restored by AST administration. There was close to no obvious difference between the IR + AST group and the Con group. Our results indicated that AST administration could prevent IR-induced microarchitecture deterioration in IR mice.

AST improves bone biomechanical strength in IR mice

To determine whether AST administration could improve bone biomechanical strength in IR mice, bone biomechanical indices were examined. In comparison with the Con group, significant decreases in biomechanical parameters were observed in the IR group, including energy absorption, yield displacement, maximum load, yield load, stiffness, ultimate displacement, tissue-level hardness, and modulus (Fig. 1C). Interestingly, these parameters were normalized by AST administration. These results demonstrated that AST could improve bone biomechanical strength in IR mice.

AST attenuates the reduction in osteoblastic bone formation in IR mice

Next, osteoblastogenesis was assessed by HE (Fig. 2A), toluidine blue (Fig. 2B), ALP (Fig. 2C), total collagen (Fig. 2D), and von Kossa (Fig. 2E) staining. We observed that there was a significant reduction in trabecular bone volume, N.ob/bs, ALP positive area/total area, total collagen positive area/total area, and von Kossa positive area/total area in the IR mice (Fig. 2G). Furthermore, dynamic histomorphometric analysis *via* calcein double labeling (Fig. 2F) revealed that the IR mice showed lower MAR, MS/BS, and BFR levels than the Con group mice (Fig. 2G). IR also led to a decrease in the serum ALP and P1NP levels (bone formation markers) compared with the Con group (Fig. 2H). ALP, BMP-2, COL-1, OCN, OSX, and Runx2 are well-known osteoblast differentiation and mineralization marker genes.[39,42,43] IR decreased the mRNA and protein expressions of ALP, BMP-2, OCN, COL-1, OSX, and Runx2 compared with the Con group (Fig. 2I and J). In addition, the protein expression levels of SOST, a potent inhibitor of Wnt signaling, increased significantly in the IR mice compared with the Con group mice (Fig. 2J). This indicated that there was decreased osteogenic activity after radiation exposure. However, these

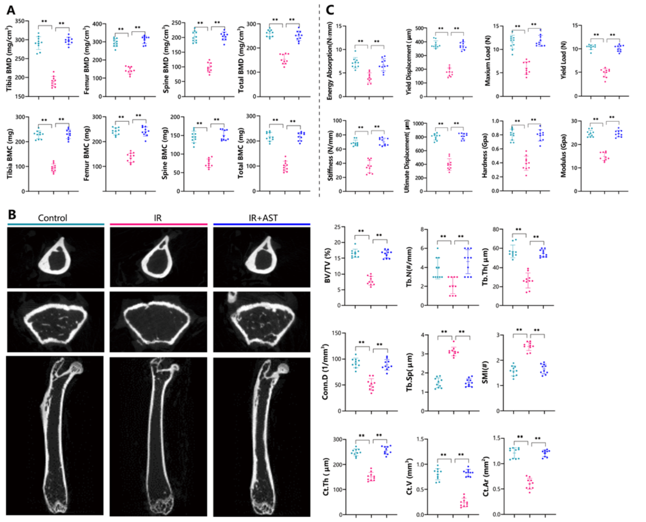

Fig. 1 AST attenuates bone mass loss in IR mice. (A) The BMD and BMC values of the tibia, femur, spine, and total body were measured by DXA. (B) Representative μCT images of the left femurs of different groups and analysis of the distal femoral bone parameters by μCT, including BV/TV, Tb.N, Tb.Th, Conn.D, Tb.Sp, SMI, Ct.Th, Ct.V, and Ct.Ar. (C) The three-point bending results of the left femurs including energy absorption, yield displacement, maximum load, yield load, stiffness, and ultimate displacement. The femoral intrinsic biomechanical material properties *via* nanoindentation testing including tissue-level hardness and modulus. The values are expressed as mean ± SD, n = 10 per group. *, $P < 0.05$; **, $P < 0.01$; and ***, $P < 0.001$ *versus* the indicated group.

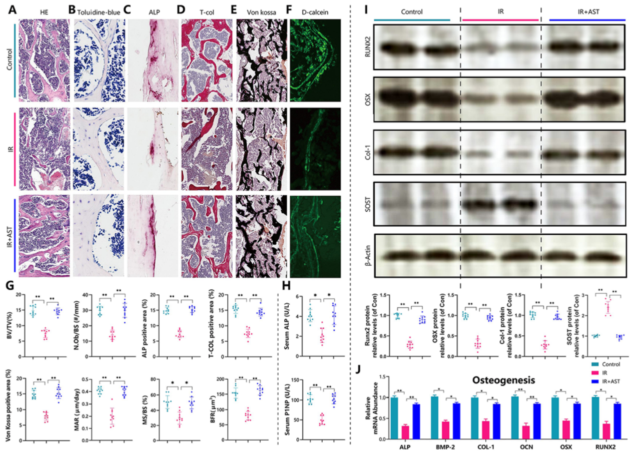

Fig. 2 AST attenuates the reduction in osteoblastic bone formation in IR mice. Osteoblastogenesis was assessed by (A) HE, (B) toluidine blue, (C) ALP, (D) total collagen, and (E) von Kossa staining. Histomorphometric analysis for (G) trabecular bone volume, N.ob/bs, ALP positive area/total area, total collagen positive area/total area, and von Kossa positive area/total area. Dynamic histomorphometric analysis *via* (F) calcein double labeling. Serum (H) ALP and P1NP were measured by ELISA. (I) The protein expression levels of RUNX2, OSX, Col-1, and SOST were detected by western blotting. β-actin was used as an internal control. (J) Real-time RT-PCR was performed to determine the mRNA expression of genes related to osteogenesis in the left tibia. The values are expressed as mean ± SD, n = 10 per group. *, $P < 0.05$; **, $P < 0.01$; and ***, $P < 0.001$ *versus* the indicated group.

parameters were normalized by AST administration. These results demonstrated that AST treatment attenuated IR-induced osteoporosis partly by attenuating the reduction in osteoblastic bone formation in IR mice.

AST inhibits osteoclastic bone resorption in IR mice

Osteoclastogenesis was assessed by TRAP staining (Fig. 3A). The numbers of pink-stained TRAP-positive osteoclastic cells in samples from the IR mice were higher than in samples from the Con group. N.OC/BS (Fig. 3B), ES/BS (Fig. 3C), and OC.S/BS (Fig. 3D) all significantly increased in the IR mice compared with the Con group mice. Moreover, IR resulted in sharp increases in serum TRAP-5b and CTX-I (bone resorption markers) compared with the Con group (Fig. 3E and F). In addition, the gene expression levels of cathepsin K (CTSK), TRAP, and RANKL all increased significantly, while OPG decreased in the IR mice compared with the Con group mice (Fig. 3G). Our data indicated increased ongoing bone resorption. However, these parameters were normalized by AST administration. These results demonstrated that IR-induced bone loss rescued by AST was associated with reduced osteoclastic bone resorption in IR mice.

AST inhibits oxidative stress in IR mice

To determine whether the IR-induced osteoporosis prevented by AST administration was interrelated with the reduced oxidative stress induced by IR, we examined the alterations in the parameters of oxidative stress and the antioxidant enzyme activity and expression levels in the three different mouse

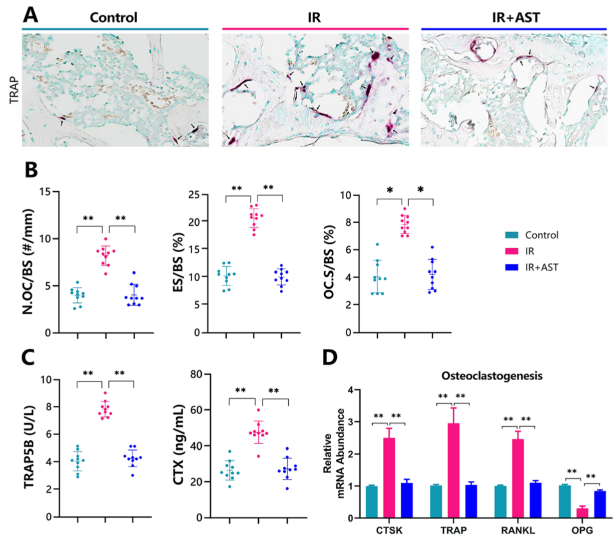

Fig. 3 AST inhibits osteoclastic bone resorption in IR mice. (A) Osteoclastogenesis was assessed by TRAP staining. (B) Histomorphometric analysis for N.OC/BS, ES/BS, and OC.S/BS. (C) Serum TRAP-5b and CTX-I were measured by ELISA. (D) Real-time RT-PCR was performed to determine the mRNA expression of genes related to osteoclastogenesis. Values are expressed as mean ± SD, n = 10 per group. *, $P < 0.05$; **, $P < 0.01$; and ***, $P < 0.001$ *versus* the indicated group.

groups. Our results showed that the gene expression levels of the antioxidant enzymes SOD1/2, GPX1/2, GSR, Txnrd1, Prx2/4, HO1, catalase, NQO1, Nrf2, and klotho in osseous tissue decreased significantly in the IR mice compared with the Con group mice (Fig. 4A). IHC staining of 8-OHdG, a sensitive indicator of oxidative stress, was markedly higher in the IR mice than in the Con mice (Fig. 4B). The protein expression levels of antioxidant enzymes including Sirt1, Prdx1, and SOD1 decreased significantly in the IR mice compared with the Con group mice (Fig. 4C). We also examined the ROS levels in bone marrow cells, spleen, and thymus. We found that the ROS levels were increased in bone marrow cells, the spleen, and the thymus (Fig. 4D). The serum malondialdehyde (MDA) content increased significantly, whereas serum total antioxidant capacity (T-AOC) and superoxide dismutase (SOD) activity were significantly reduced in the IR mice compared with the Con group mice (Fig. 4E). However, these parameters were normalized by AST administration. These results showed that IR could induce oxidative stress in bony tissue, whereas AST administration reduced oxidative stress in IR mice.

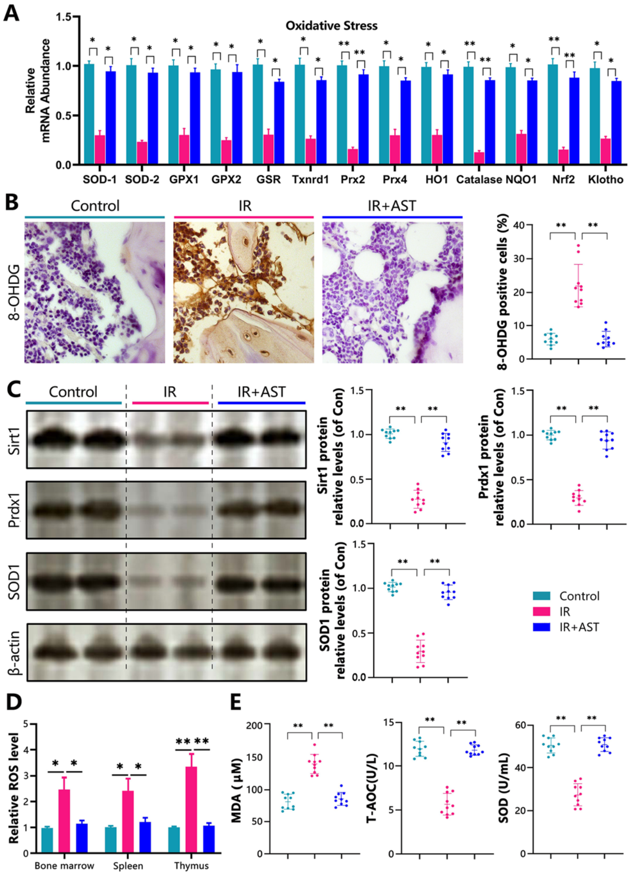

Fig. 4 AST inhibits oxidative stress in IR mice. (A) Real-time RT-PCR was performed to determine the mRNA expression of genes related to oxidative stress in osseous tissue. (B) IHC staining of 8-OHdG, a sensitive indicator of oxidative stress. (C) The protein expression levels of antioxidant enzymes including Sirt1, Prdx1, and SOD1 were detected by western blotting. β-Actin was used as an internal control. (D) ROS levels in bone marrow cells, spleen, and thymus. (E) Serum MDA, total antioxidant capacity (T-AOC) and superoxide dismutase (SOD) activity were measured by ELISA. The values are expressed as mean ± SD, $n = 10$ per group. *, $P < 0.05$; **, $P < 0.01$; and ***, $P < 0.001$ *versus* the indicated group.

AST inhibits DNA damage in IR mice

Our previous study demonstrated that mice subjected to radiation exposure exhibited DNA damage.[44] To investigate whether this situation occurred in bone, the DNA damage marker γH2AX was examined by western blotting using bone samples from different mice. Results revealed that the protein expression of γ-H2AX significantly increased in the IR mice compared with the Con mice (Fig. 5A). These observations implied that IR induced DNA damage and AST inhibited DNA damage in IR mice.

AST inhibits osteocyte senescence and SASP in IR mice

To examine whether the IR-induced bone loss prevented by AST administration was associated with cellular senescence, we quantified the alterations in osteocyte senescence and SASP. We found that the percentages of p16 (Fig. 5B), p21 (Fig. 5C), p53 (Fig. 5D), and SA-β-gal (Fig. 5E) positive osteocytes all increased significantly in the IR mice compared with the Con group mice. Consistent with this, the protein expression levels of p16, p21, and p53 (Fig. 5F) all increased significantly in the IR mice compared with the Con group mice. In addition, the gene expression levels of SASP markers,

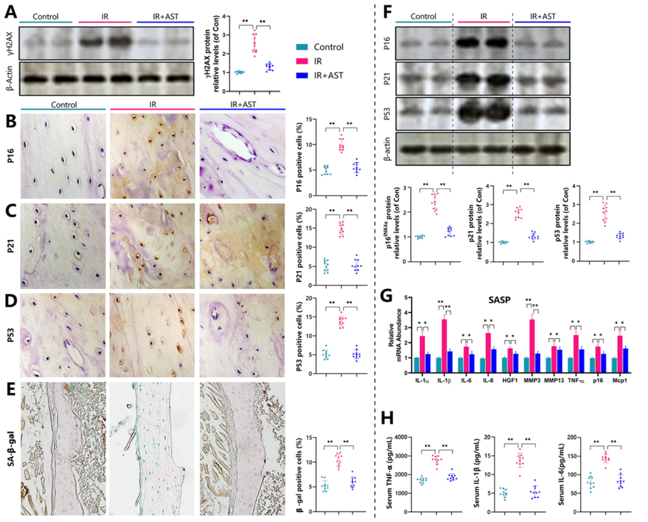

Fig. 5 AST inhibits DNA damage, osteocyte senescence, and SASP in IR mice. (A) The protein expression of γ-H2AX was detected by western blotting. β-Actin was used as an internal control. Representative micrographs from paraffin sections of distal femurs with IHC staining for (B) p16, (C) p21, (D) p53, and (E) SA-β-gal. (F) The protein expression levels of p16, p21, and p53 were detected by western blotting. β-Actin was used as an internal control. (G) Real-time RT-PCR was performed to determine the mRNA expression of genes related to SASP. (H) Serum TNF-α, IL-1β, and IL-6 are measured by ELISA. Values are expressed as mean ± SD, $n = 10$ per group. *, $P < 0.05$; **, $P < 0.01$; and ***, $P < 0.001$ *versus* the indicated group.

including IL-1α, IL-1β, IL-6, IL-8, HGF1, Mmp3, Mmp13, TNF-α, P16, and Mcp1, all significantly increased in the IR mice compared with the Con group mice (Fig. 5G). Serum TNF-α, IL-1β, and IL-6 levels all increased significantly in the IR mice compared with the Con group mice (Fig. 5H). However, these parameters were normalized by AST administration. These results clearly demonstrated that IR induced osteocyte senescence and SASP, whereas AST administration inhibited osteocyte senescence and SASP in the IR mice.

Discussion

As a pivotal clinical therapy to treat cancer, RT can also damage adjacent tissues.[1] The adverse effects of RT, including bone damage, are unavoidable side effects of this treatment and may lead to radiation-induced bone loss, reductions in bone biomechanical strength, and increased risk of fragility fractures.[3,5,7,45,46] The radiation-exposure mouse model is a well-established animal model for studying IR-induced osteoporosis.[16,39] In this study, we used an IR mouse model to determine the effects of AST on IR-induced osteoporosis. Our study demonstrated that IR not only increased osteoclastic bone resorption but also decreased osteoblastic bone formation and bone biomechanical strength. In contrast, nearly all these parameters were normalized by AST administration. We also demonstrated the anti-osteoporosis role of AST, which functioned by upregulating antioxidant capacity, suppressing oxidative stress and lowering DNA damage levels, and inhibiting osteocyte senescence and SASP secretion.

It is widely accepted that IR increases oxidative stress, which contributes to IR-related tissue injury. IR may quickly cause the decomposition of water, forming a great amount of oxygen free radicals[47] that impair normal cells and tissues.[46–48] Recent studies strongly indicate that IR severely impairs the defense mechanisms of antioxidant stress responses and accelerates bone aging.[41,49] Supplementation with antioxidants is a useful approach to mitigate the damage caused by excessive ROS and cell senescence.[50] Studies in our laboratory have also shown that pyrroloquinoline quinone (PQQ), a powerful antioxidant, prevents estrogen-deficiency-induced osteoporosis due to its impact on ROS levels and inhibits cell senescence and SASP secretion.[42] In this study, the level of ROS in the bone marrow, spleen, and thymus increased significantly after IR exposure (Fig. 4D). Excessive generation of ROS can damage the cell membrane and cytoplasm and ultimately leads to DNA damage.[51] Consistent with this, our current study also demonstrated that the DNA damage marker γH2AX was increased by IR (Fig. 5A), suggesting that IR may result in increased DNA damage. Moreover, the gene (SOD1, SOD2, Gpx1, Gpx2, GSR, Txnrd1, Prx-2, Prx-4, HO1, catalase, NQO1, Nrf2, and klotho) and protein (SOD1, SOD2, and Sirt1) expression levels of the antioxidant enzymes in osseous tissue were downregulated in IR mice (Fig. 4A and C). Nrf2 is a redox-sensitive transcription factor. Nrf2 can activate many genes encoding for detoxifying and antioxidant enzymes such as catalase, SOD1, SOD2, peroxiredoxins (Prx), haem oxygenase 1 (HO1), glutamate-cysteine ligase (GCL), and NADPH quinone oxidase 1 (NQO1).[52] Klotho is an anti-aging gene. A previous study reported that klotho significantly enhanced the expression of the Trx/Prx system that acts to attenuate ROS production.[53] Klotho mutant mice (C3H) were found to be strongly associated with a remarkable increase in oxidative stress markers.[54] Coincidentally, several studies have shown that the expressions of Nrf2 and klotho were both regulated by radiation exposure,[41,55] suggesting that radiation exposure acting in conjunction with klotho and Nrf2 regulates the expression of many of the antioxidant systems that prevent oxidative stress by removing ROS. Our data indicated that radiation exposure induced an increase in ROS formation, resulting from the reduction of antioxidant gene expression by downregulating Nrf2 and klotho.

Senescent cells are distinct from quiescent and terminally differentiated cells in that they develop a unique phenotypic signature, characterized by profound chromatin and secretome changes typically induced by nuclear DNA damage and mitochondrial dysfunction.[22,56,57] Mitochondrial dysfunction is a major characteristic of cellular senescence, and dysfunctional mitochondria occupy a central position in the development of SASP. Mitochondrial distress-induced cGAS/STING activation has been implicated as a crucial mechanism underlying macrophage hyperactivation, exacerbated inflammapathology, and SASP production. Accordingly, the inhibition of the STING pathway or, more strikingly, the elimination of senescent macrophages by senolytics alleviated pathogenic inflammation.[58,59] Senescent cells can secrete SASP that has harmful paracrine and systemic effects.[25–27] The accumulation of senescent cells and SASP causes deleterious changes in tissue remodeling and leads to tissue dysfunction. The use of a SASP inhibitor (Ruxolitinib)[29] or a senolytic cocktail of dasatinib and quercetin (D + Q) enhanced bone accrual in old mice. We showed previously that in an INK-ATTAC transgenic rodent model, cell clearance of 30% of senescent cells had convincing effects on the prevention of numerous age-associated comorbidities.[60] Thus, reducing SASP secretion by senomorphic agents and clearance of senescent cells by senolytic agents may be viable therapies that can potentially improve bone integrity and function.[58,59,61–63]

Our results show that AST was beneficial for preventing IR-induced osteoporosis by inhibiting osteoclastic bone resorption (Fig. 3), stimulating osteoblastic bone formation (Fig. 2) and enhancing bone strength (Fig. 1C). Thus, we asked whether the IR-induced bone loss prevented by AST administration was associated with reduced osteocyte senescence and SASP induced by IR. As expected, we found that IR could induce osteocyte senescence as shown by the higher expression levels of senescence marker proteins including p16INK4a, p21, p53, and SA-β-gal (Fig. 5F), and the percentage of osteocytes positively stained for those factors all increased significantly in bone from the IR mice compared with the control mice (Fig. 5B–E).[64] We also found that IR increased the expression of SASP genes, including Ccl2, Ccl4, Ccl5, Ccl7, Cxcl1, Cxcl2, Cxcl3, Cxcl4, Cxcr5, IL-1α, IL-1β, IL-6, IL-8, IL-10, IL-18, Mmp-2, Mmp-3, and Mmp-13.[18,42] Our findings support the notion that IR may induce oxidative stress to cause DNA damage ultimately leading to a senescence phenotype in osteocytes and SASP. Interestingly, nearly all results from IR treatment were normalized by AST administration. Therefore, our results suggest that AST treatment can inhibit the osteocyte senescence and SASP secretion induced by IR.

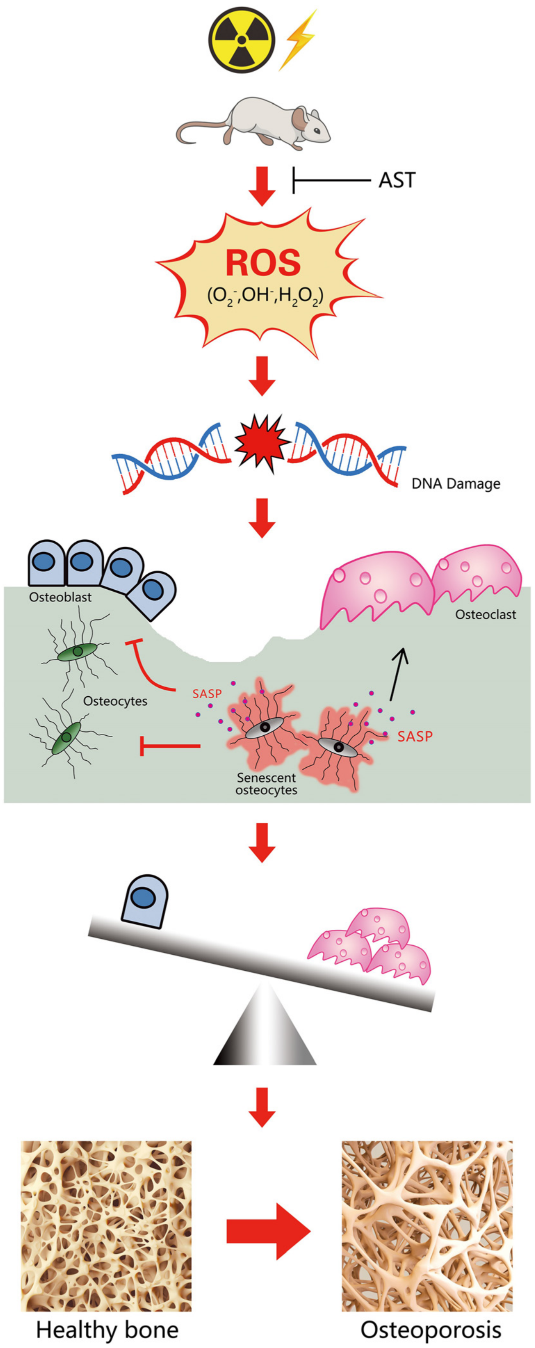

Fig. 6 A schematic diagram showing the mechanism of AST attenuating irradiation-induced osteoporosis in mice by inhibiting oxidative stress, osteocytes senescence, and SASP.

Conclusions

In conclusion, our study demonstrated that IR induced oxidative stress to cause DNA damage, ultimately leading to a senescence phenotype in osteocytes. IR-induced osteoporosis was related not only to promoted osteoclastic bone resorption but also to decreased osteoblastic bone formation. We demonstrated here that AST had preventative effects against IR-induced osteoporosis in mice. The underlying mechanisms may involve inhibiting oxidative stress and preventing osteocyte senescence and SASP secretion (Fig. 6). Therefore, our results provide new insights into the regulation of osteoporosis and suggest a novel strategy for the prevention and treatment of IR-related bone loss.

Author contributions

Qinghe Geng wrote this article; Qinghe Geng, Shen Wang, Ke Heng, Juan Zhai, Xingchen Song, Lei Xia, and Lulu Wang carried out the experiments and interpreted the results; Qiang Lin and Hongwei Li performed data analysis work; Qinghe Geng and Yilong Guo designed the study and interpreted the results.

Conflicts of interest

There are no conflicts to declare.

Acknowledgements

This study was supported by the Postdoctoral Research Foundation of China (Grant No. 2020M681739), the Research Funding Project of the Jiangsu Commission of Health (Grant No. Z2021046), and the Research Funding Project of Xuzhou Medical University (Grant No. XZSYSKF2020004 and 2018KJ23). We thank LetPub (https://www.letpub.com) for its linguistic assistance during the preparation of this manuscript.

References

1 J. A. Horton, *et al.*, Mesenchymal stem cells inhibit cutaneous radiation-induced fibrosis by suppressing chronic inflammation, *Stem Cells*, 2013, **31**(10), 2231–2241.
2 X. Cao, *et al.*, Irradiation induces bone injury by damaging bone marrow microenvironment for stem cells, *Proc. Natl. Acad. Sci. U. S. A.*, 2011, **108**(4), 1609–1614.
3 D. E. Green, *et al.*, Devastation of adult stem cell pools by irradiation precedes collapse of trabecular bone quality and quantity, *J. Bone Miner. Res.*, 2012, **27**(4), 749–759.
4 K. C. Yerit, *et al.*, Implant survival in mandibles of irradiated oral cancer patients, *Clin. Oral Implants Res.*, 2006, **17**(3), 337–344.

5 H. Kondo, *et al.*, Total-body irradiation of postpubertal mice with (137)Cs acutely compromises the microarchitecture of cancellous bone and increases osteoclasts, *Radiat. Res.*, 2009, **171**(3), 283–289.

6 J. S. Willey, *et al.*, Early increase in osteoclast number in mice after whole-body irradiation with 2 Gy X rays, *Radiat. Res.*, 2008, **170**(3), 388–392.

7 J. S. Willey, *et al.*, Risedronate prevents early radiation-induced osteoporosis in mice at multiple skeletal locations, *Bone*, 2010, **46**(1), 101–111.

8 E. R. Bandstra, *et al.*, Long-term dose response of trabecular bone in mice to proton radiation, *Radiat. Res.*, 2008, **169**(6), 607–614.

9 D. Jia, *et al.*, Rapid loss of bone mass and strength in mice after abdominal irradiation, *Radiat. Res.*, 2011, **176**(5), 624–635.

10 S. A. Hamilton, *et al.*, A murine model for bone loss from therapeutic and space-relevant sources of radiation, *J. Appl. Physiol.*, 2006, **101**(3), 789–793.

11 J. D. Wernle, *et al.*, Local irradiation alters bone morphology and increases bone fragility in a mouse model, *J. Biomech.*, 2010, **43**(14), 2738–2746.

12 J. H. Hwang, *et al.*, Bone mineral density after concurrent chemoradiation in patients with uterine cervical cancer, *Menopause*, 2010, **17**(2), 416–420.

13 J. E. Wall, *et al.*, Fractures in children treated with radiotherapy for soft tissue sarcoma, *Orthopedics*, 1996, **19**(8), 657–664.

14 K. M. Schmeler, *et al.*, Pelvic fractures after radiotherapy for cervical cancer: implications for survivors, *Cancer*, 2010, **116**(3), 625–630.

15 J. W. Hopewell, Radiation-therapy effects on bone density, *Med. Pediatr. Oncol.*, 2003, **41**(3), 208–211.

16 A. Chandra, S. S. Park and R. J. Pignolo, Potential role of senescence in radiation-induced damage of the aged skeleton, *Bone*, 2019, **120**, 423–431.

17 J. N. Farr, *et al.*, Identification of Senescent Cells in the Bone Microenvironment, *J. Bone Miner. Res.*, 2016, **31**(11), 1920–1929.

18 A. Chandra, *et al.*, Targeted Reduction of Senescent Cell Burden Alleviates Focal Radiotherapy-Related Bone Loss, *J. Bone Miner. Res.*, 2020, **35**(6), 1119–1131.

19 T. Tchkonia, *et al.*, Cellular senescence and the senescent secretory phenotype: therapeutic opportunities, *J. Clin. Invest.*, 2013, **123**(3), 966–972.

20 J. M. van Deursen, The role of senescent cells in ageing, *Nature*, 2014, **509**(7501), 439–446.

21 B. G. Childs, *et al.*, Cellular senescence in aging and age-related disease: from mechanisms to therapy, *Nat. Med.*, 2015, **21**(12), 1424–1435.

22 E. C. Swanson, *et al.*, Higher-order unfolding of satellite heterochromatin is a consistent and early event in cell senescence, *J. Cell Biol.*, 2013, **203**(6), 929–942.

23 E. Wang, Senescent human fibroblasts resist programmed cell death, and failure to suppress bcl2 is involved, *Cancer Res.*, 1995, **55**(11), 2284–2292.

24 J. P. Coppé, *et al.*, Senescence-associated secretory phenotypes reveal cell-nonautonomous functions of oncogenic RAS and the p53 tumor suppressor, *PLos Biol.*, 2008, **6**(12), 2853–2868.

25 J. C. Acosta, *et al.*, A complex secretory program orchestrated by the inflammasome controls paracrine senescence, *Nat. Cell Biol.*, 2013, **15**(8), 978–990.

26 J. P. Coppé, *et al.*, The senescence-associated secretory phenotype: the dark side of tumor suppression, *Annu. Rev. Phytopathol.*, 2010, **5**, 99–118.

27 G. Nelson, *et al.*, A senescent cell bystander effect: senescence-induced senescence, *Aging Cell*, 2012, **11**(2), 345–349.

28 N. A. Sims, Senescent Osteocytes: Do They Cause Damage and Can They Be Targeted to Preserve the Skeleton?, *J. Bone Miner. Res.*, 2016, **31**(11), 1917–1919.

29 J. N. Farr, *et al.*, Targeting cellular senescence prevents age-related bone loss in mice, *Nat. Med.*, 2017, **23**(9), 1072–1079.

30 R. T. Lorenz and G. R. Cysewski, Commercial potential for Haematococcus microalgae as a natural source of astaxanthin, *Trends Biotechnol.*, 2000, **18**(4), 160–167.

31 P. Kidd, Astaxanthin, cell membrane nutrient with diverse clinical benefits and anti-aging potential, *Altern. Med. Rev.*, 2011, **16**(4), 355–364.

32 S. Li, *et al.*, Astaxanthin prevents ischemia-reperfusion injury of the steatotic liver in mice, *PLoS One*, 2017, **12**(11), e0187810.

33 Y. H. Hwang, *et al.*, The Protective Effects of Astaxanthin on the OVA-Induced Asthma Mice Model, *Molecules*, 2017, **22**(11), 2019.

34 J. Zhang, *et al.*, Astaxanthin pretreatment attenuates acetaminophen-induced liver injury in mice, *Int. Immunopharmacol.*, 2017, **45**, 26–33.

35 X. Wen, *et al.*, Astaxanthin acts via LRP-1 to inhibit inflammation and reverse lipopolysaccharide-induced M1/M2 polarization of microglial cells, *Oncotarget*, 2017, **8**(41), 69370–69385.

36 Y. Naito, *et al.*, Microarray profiling of gene expression patterns in glomerular cells of astaxanthin-treated diabetic mice: a nutrigenomic approach, *Int. J. Mol. Med.*, 2006, **18**(4), 685–695.

37 H. Balci Yuce, *et al.*, Investigation of the effect of astaxanthin on alveolar bone loss in experimental periodontitis, *J. Periodontal Res.*, 2018, **53**(1), 131–138.

38 Y. H. Hwang, *et al.*, Suppression Effect of Astaxanthin on Osteoclast Formation In Vitro and Bone Loss In Vivo, *Int. J. Mol. Sci.*, 2018, **19**(3), 912.

39 S. Wang, *et al.*, Treatment with soluble bone morphogenetic protein type 1A receptor fusion protein alleviates irradiation-induced bone loss in mice through increased bone formation and reduced bone resorption, *Am. J. Transl. Res.*, 2020, **12**(3), 743–757.

40 H. Hoshi, *et al.*, Astaxanthin improves osteopenia caused by aldehyde-stress resulting from Aldh2 mutation due to impaired osteoblastogenesis, *Biochem. Biophys. Res. Commun.*, 2020, **527**(1), 270–275.

41 T. Rana, *et al.*, Loss of Nrf2 accelerates ionizing radiation-induced bone loss by upregulating RANKL, *Free Radicals Biol. Med.*, 2012, **53**(12), 2298–2307.

42 Q. Geng, *et al.*, Pyrroloquinoline Quinone Prevents Estrogen Deficiency-Induced Osteoporosis by Inhibiting Oxidative Stress and Osteocyte Senescence, *Int. J. Biol. Sci.*, 2019, **15**(1), 58–68.

43 Q. Geng, *et al.*, A soluble bone morphogenetic protein type 1A receptor fusion protein treatment prevents glucocorticoid-Induced bone loss in mice, *Am. J. Transl. Res.*, 2019, **11**(7), 4232–4247.

44 I. R. Miousse, *et al.*, Exposure to low-dose (56)Fe-ion radiation induces long-term epigenetic alterations in mouse bone marrow hematopoietic progenitor and stem cells, *Radiat. Res.*, 2014, **182**(1), 92–101.

45 B. Yang, *et al.*, Effect of radiation on the expression of osteoclast marker genes in RAW264.7 cells, *Mol. Med. Rep.*, 2012, **5**(4), 955–958.

46 J. S. Willey, *et al.*, Ionizing Radiation and Bone Loss: Space Exploration and Clinical Therapy Applications, *Clin. Rev. Bone Miner. Metab.*, 2011, **9**(1), 54–62.

47 P. A. Riley, Free radicals in biology: oxidative stress and the effects of ionizing radiation, *Int. J. Radiat. Biol.*, 1994, **65**(1), 27–33.

48 D. Mukherjee, *et al.*, Responses to ionizing radiation mediated by inflammatory mechanisms, *J. Pathol.*, 2014, **232**(3), 289–299.

49 A. Gajowik and M. M. Dobrzyńska, Lycopene - antioxidant with radioprotective and anticancer properties. A review, *Rocz. Panstw. Zakl. Hig.*, 2014, **65**(4), 263–271.

50 K. Thirumurugan, Senolytic Phytocompounds in Redox Signaling, in *Redox Signaling and Biomarkers in Ageing*, ed. U. Çakatay, Springer International Publishing, Cham, 2022, pp. 255–283.

51 W. Dröge, Free radicals in the physiological control of cell function, *Physiol. Rev.*, 2002, **82**(1), 47–95.

52 J. D. Hayes and A. T. Dinkova-Kostova, The Nrf2 regulatory network provides an interface between redox and intermediary metabolism, *Trends Biochem. Sci.*, 2014, **39**(4), 199–218.

53 E. Zeldich, *et al.*, The neuroprotective effect of Klotho is mediated via regulation of members of the redox system, *J. Biol. Chem.*, 2014, **289**(35), 24700–24715.

54 T. Nagai, *et al.*, Cognition impairment in the genetic model of aging klotho gene mutant mice: a role of oxidative stress, *FASEB J.*, 2003, **17**(1), 50–52.

55 D. Y. Kim, M. Lee and E. J. Kim, Involvement of Klotho, TNF-α and ADAMs in radiation-induced senescence of renal epithelial cells, *Mol. Med. Rep.*, 2021, **23**(1), 1.

56 T. von Zglinicki, *et al.*, Human cell senescence as a DNA damage response, *Mech. Ageing Dev.*, 2005, **126**(1), 111–117.

57 D. V. Ziegler, C. D. Wiley and M. C. Velarde, Mitochondrial effectors of cellular senescence: beyond the free radical theory of aging, *Aging Cell*, 2015, **14**(1), 1–7.

58 M. C. Atayik and U. Çakatay, Mitochondria-targeted senotherapeutic interventions, *Biogerontology*, 2022, **23**(4), 401–423.

59 M. Conte, *et al.*, Mitochondria, immunosenescence and inflammaging: a role for mitokines?, *Semin. Immunopathol.*, 2020, **42**(5), 607–617.

60 D. J. Baker, *et al.*, Clearance of p16Ink4a-positive senescent cells delays ageing-associated disorders, *Nature*, 2011, **479**(7372), 232–236.

61 Q. Geng, *et al.*, Lycopene Protects Against Glucocorticoid-Induced Osteoporosis In Mice: Impact On Oxidative Stress And Osteocyte Senescence, *J. Bone Miner. Res.*, 2019, **34**, 217–217.

62 Q. Geng, *et al.*, Overexpression of Sirt1 in Mesenchymal Stem Cells Protects against Glucocorticoid-Induced Osteoporosis by Inhibiting Oxidative Stress and Osteocyte Senescence, *J. Bone Miner. Res.*, 2018, **33**, 80–81.

63 Q. Geng, *et al.*, Pyrroloquinoline Quinone Prevents Estrogen Deficiency-Induced Osteoporosis by Inhibiting Oxidative Stress and Osteocyte Senescence, *Int. J. Biol. Sci.*, 2019, **15**(1), 58–68.

64 M. Althubiti, *et al.*, Characterization of novel markers of senescence and their prognostic potential in cancer, *Cell Death Discovery*, 2014, **5**(11), e1528.